Extreme plastic deformation and subsequent Pb loss in shocked xenotime from the Vredefort Dome, South Africa

The Geological Society of America
Special Paper 550

Extreme plastic deformation and subsequent Pb loss in shocked xenotime from the Vredefort Dome, South Africa

Aaron J. Cavosie
School of Earth and Planetary Sciences, Space Science and Technology Centre, The Institute for Geoscience Research, Curtin University, Perth, WA 6102, Australia

Christopher L. Kirkland
School of Earth and Planetary Sciences, Timescales of Mineral Systems Group, The Institute for Geoscience Research, Curtin University, Perth, WA 6102, Australia

Steven M. Reddy
School of Earth and Planetary Sciences, Geoscience Atom Probe Facility, The Institute for Geoscience Research, Curtin University, Perth, WA 6102, Australia

Nicholas E. Timms
School of Earth and Planetary Sciences, Space Science and Technology Centre, The Institute for Geoscience Research, Curtin University, Perth, WA 6102, Australia

Cristina Talavera
School of Earth and Planetary Sciences, John de Laeter Centre, The Institute for Geoscience Research, Curtin University, Perth, WA 6102, Australia, and
School of Geosciences, University of Edinburgh, The King's Building, James Hutton Road, Edinburgh EH9 3FE, UK

Maya R. Pincus

American Museum of Natural History, New York, New York 10024, USA

ABSTRACT

Accessory mineral U-Pb geochronometers are crucial tools for constraining the timing of deformation in a wide range of geological settings. Despite the growing recognition that intragrain age variations within deformed minerals can spatially correlate to zones of microstructural damage, the causal mechanisms of Pb loss are not always evident. Here, we report the first U-Pb data for shock-deformed xenotime, from a detrital grain collected at the Vredefort impact structure in South Africa. Orientation mapping revealed multiple shock features, including pervasive planar deformation bands (PDBs) that accommodate up to 40° of lattice misorientation by <100>{010} slip, and also an ~50-µm-wide intragrain shear zone that contains {112}

Cavosie, A.J., Kirkland, C.L., Reddy, S.M., Timms, N.E., Talavera, C., and Pincus, M.R., 2021, Extreme plastic deformation and subsequent Pb loss in shocked xenotime from the Vredefort Dome, South Africa, *in* Reimold, W.U., and Koeberl, C., eds., Large Meteorite Impacts and Planetary Evolution VI: Geological Society of America Special Paper 550, p. 1–14, https://doi.org/10.1130/2021.2550(20).

deformation twin lamellae in two orientations. Twenty-nine in situ secondary ion mass spectrometry (SIMS) U-Pb analyses from all microstructural domains yielded a well-defined discordia with upper-intercept age of 2953 ± 15 Ma (mean square of weighted deviation [MSWD] = 0.57, *n* = 29, 2σ), consistent with derivation from Kaapvaal craton bedrock. However, the 1754 ± 150 Ma lower concordia intercept age falls between the 2020 Ma Vredefort impact and ca. 1100 Ma Kibaran orogenesis and is not well explained by multiple Pb-loss episodes. The pattern and degree of Pb loss (discordance) correlate with increased [U] but do not correlate to microstructure (twin, PDB) or to crystallinity (band contrast) at the scale of SIMS analysis. Numerical modeling of the Pb-loss history using a concordia-discordia-comparison (CDC) test indicated that the lower concordia age is instead best explained by an alteration episode at ca. 1750 Ma, rather than a multiple Pb-loss history. In this example, the U-Pb system in deformed xenotime does not record a clear signature of impact age resetting; rather, the implied high dislocation density recorded by planar deformation bands and the presence of deformation twins facilitated subsequent Pb loss during a younger event that affected the Witwatersrand basin. Microstructural characterization of xenotime targeted for geochronology provides a new tool for recognizing evidence of deformation and can provide insight into complex age data from highly strained grains, and, as is the case in this study, elucidate previously unrecognized alteration events.

DEFORMATION AND U-Pb GEOCHRONOLOGY OF XENOTIME

Xenotime is a Y + rare earth element (REE) phosphate mineral that is increasingly being utilized in U-Pb studies for dating crystallization and diagenesis, because it typically contains thousands of parts per million U (Hawkins and Bowring, 1997; Rasmussen, 2005), and Pb loss by volume diffusion in xenotime is slower than for zircon and monazite (Cherniak, 2006). Despite its use as a U-Pb geochronometer, no studies have characterized Pb loss in deformed xenotime. Information on deformation of xenotime is based mostly on experimental indentation studies of phosphates synthesized for manufacturing (Hay et al., 2013; Wilkinson et al., 2017); only recently has naturally occurring crystal-plastic deformation of xenotime been described (Cavosie et al., 2016; Cox et al., this volume). The response of the U-Pb system in deformed xenotime is unknown, but it is needed to provide a framework for interpreting geochronological data for deformed grains from various environments. Here, we present microstructural and geochronological data to evaluate the response of the U-Pb system in a shocked xenotime grain from the Vredefort Dome in the Witwatersrand basin of South Africa, the erosional remnant of a giant impact structure. The ca. 2020 Ma age of the Vredefort impact (Kamo et al., 1996; Gibson et al., 1997; Moser, 1997) and other regional events in the Witwatersrand basin are generally well constrained and thus provide an established temporal framework for interpreting deformed xenotime U-Pb systematics.

SAMPLES AND METHODS

The xenotime grain analyzed, 14VD64-1, was collected as modern colluvium in the "collar" area of the Vredefort structure (Fig. 1). The collar area consists of mostly supracrustal rocks that are part of the central uplift of the impact structure (Gibson and Reimold, 2008). The sampling site is on Buffelskloof farm (26°51.176′S, 27°16.691′E). The site is within the ~10 GPa isobar defined by the lower limit of planar deformation features (PDFs) in shocked quartz, which is locally abundant (e.g., Carter, 1965; Grieve et al., 1990; Gibson and Reimold, 2005). Shock-twinned detrital zircon grains occur in sample 14VD64 (Fig. 2) and in other samples nearby (Fig. 1B). Only one xenotime grain was recovered from the ~2 kg sediment sample. The exterior surface of the detrital xenotime grain was imaged using backscattered electron (BSE) imaging, then mounted in epoxy, further characterized (Fig. 3), and then analyzed by electron backscatter diffraction (EBSD).

Scanning electron microscopy (SEM) analysis was conducted using a Tescan MIRA3 field emission gun (FEG) SEM at the Microscopy and Microanalysis Facility of the John de Laeter Centre at Curtin University, Perth, Australia. The FEG-SEM was used for BSE imaging and EBSD analysis. Automated EBSD maps of the whole grain and regions of interest were generated by indexing EBSD patterns on user-defined grids. The whole-grain map was collected using a step size of 600 nm, whereas region of interest maps were collected using step sizes ranging from 50 to 100 nm. EBSD analyses were collected with a 20 kV accelerating voltage, 70° sample tilt, 20.5 mm working distance, and ~1 nA beam current. EBSD patterns for xenotime were collected with a Nordlys Nano high-resolution detector and Oxford Instruments AZtec system (v. 4.1) using routine data acquisition and noise reduction settings for xenotime (Table 1; Cavosie et al., 2016). EBSD patterns for zircon were collected with a Oxford Symmetry detector and Oxford Instruments AZtec system (v. 4.2) using routine data acquisition and noise reduction settings

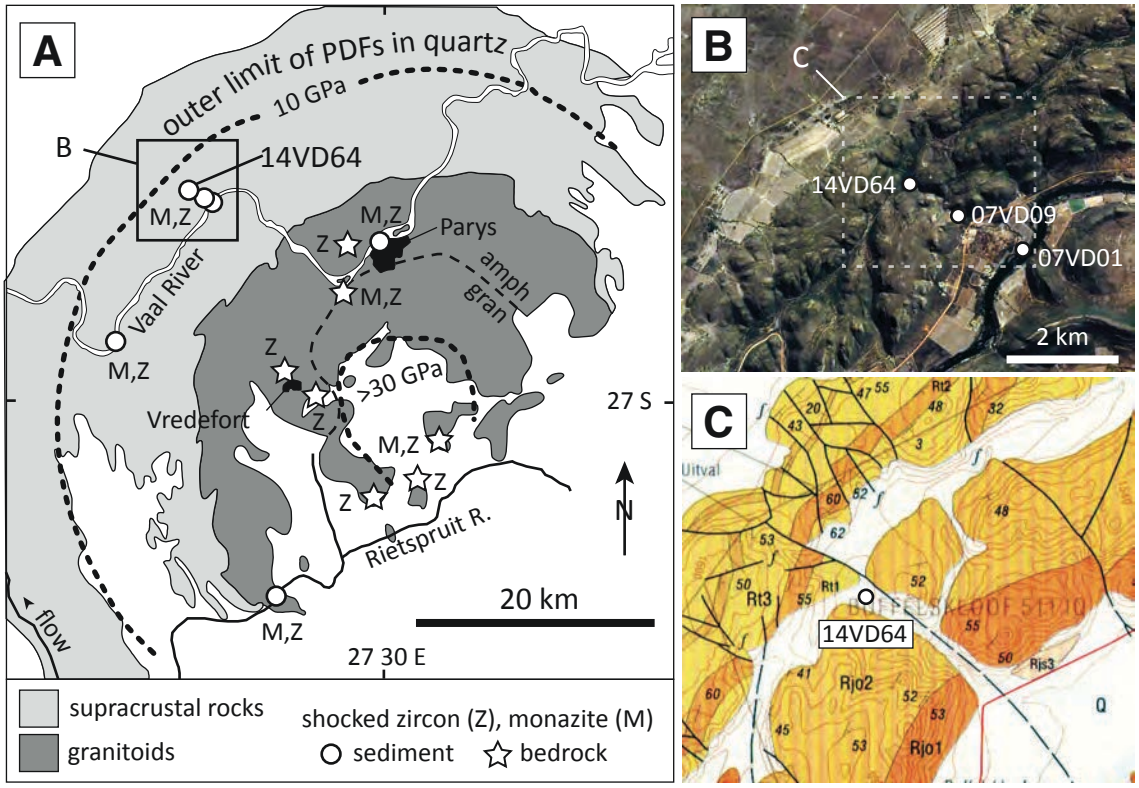

Figure 1. Sample location at the Vredefort Dome impact structure. (A) Simplified geological map of the Vredefort impact structure (after Cavosie et al., 2010). The detrital shocked xenotime grain was found in sample 14VD64, collected in the "collar" of the structure. (B) Satellite image from Google Earth™ showing the sampling locality for sample 14VD64 and two other known detrital shocked mineral localities (Cavosie et al., 2010; Erickson et al., 2016). (C) Geologic map of the area around sample 14VD64 showing stratigraphic units of the Witwatersrand Supergroup (Bischoff et al., 1999). Map units: Rjs3—slate, Jeppestown subgroup; Rjo1-2—quartzite, Johannesburg subgroup; Rt1-5—quartzite, Turffontein subgroup; Q—Quaternary sand and gravel; M—monazite; Z—zircon; amph—amphibolite; gran—granulite.

for zircon (Table 1). Energy dispersive spectroscopy (EDS) elemental maps were collected simultaneously with the EBSD data to provide additional phase identification information, because EBSD automated software systems cannot discriminate amongst EBSD patterns for certain tetragonal phases, such as zircon, xenotime, and rutile. EDS elemental data confirmed that grain 14VD64-1 was xenotime.

EBSD maps and pole figures were processed using the Tango and Mambo modules in the Oxford Instruments Channel 5 software package (v. 5.12). Several types of EBSD images are shown. Band contrast (BC) images were combined with other EBSD maps. BC images are derived from the Hough transform of the patterns and represent the contrast between the background and the high points in Hough space. In general, BC maps show the relative quality of the EBSD pattern; bright areas can be considered more crystalline, and dark areas can be considered less crystalline. Cracks, grain boundaries, radiation damage, amorphous domains, certain orientations, and areas that are poorly polished generally are dark to black in BC images because they yield either poor or no diffraction patterns. Inverse pole figure maps (IPF) show the orientation of the sample in the crystal coordinate framework of the polished sample (e.g., Fig. 2B). Pole figures (e.g., Fig. 2B) are equal-area, lower-hemisphere stereonet projections.

Secondary Ion Mass Spectrometry (SIMS) Analysis

Xenotime grain 14VD64-1 was analyzed on 13 March 2017 using a sensitive high-resolution ion microprobe (SHRIMP) II in the John de Laeter Centre, Curtin University, Perth, Australia. In total, 29 in situ U-Pb analyses were made employing a 10-µm-diameter beam width (Table 2). The secondary ion mass spectrometry (SIMS) data were calibrated against in-house Archean xenotime standard XKARG (U = 5000 ppm; age = 2641.5 Ma, provided by A. Kennedy). Sample data were matrix-corrected for U content using the calculation approach described in Fletcher et al. (2004). Fifteen analyses of the XKARG standard were obtained during the session, of which 13 indicated an external spot-to-spot (reproducibility) uncertainty of 0.87% (1σ), and a $^{238}U/^{206}Pb^*$ calibration uncertainty of 0.28% (1σ). Calibration uncertainties are included in the errors of $^{238}U/^{206}Pb^*$ ratios

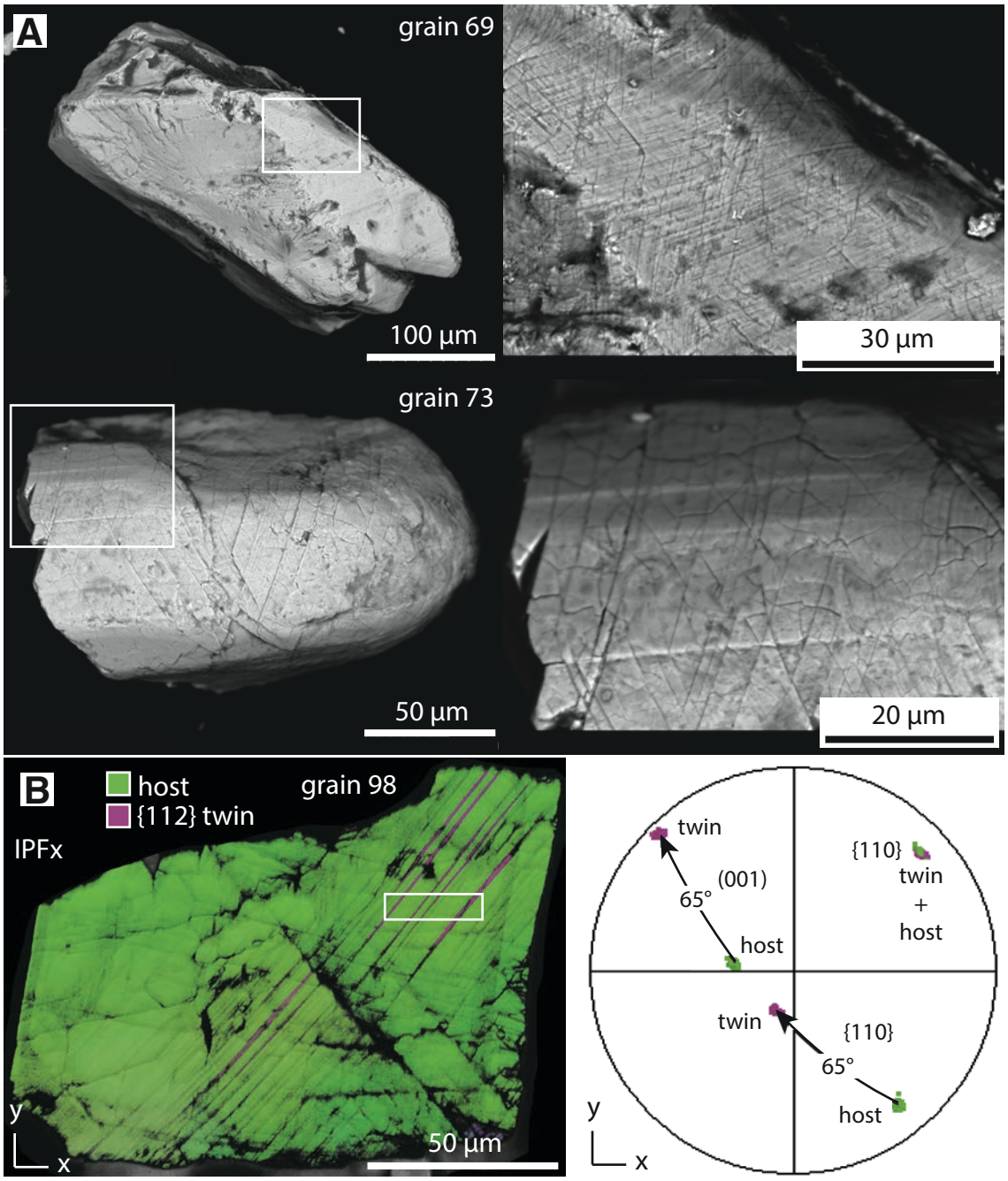

Figure 2. Detrital shocked zircons in sample 14VD64. (A) Backscattered electron images of the exterior surfaces of detrital shocked zircon grains with planar microstructures. (B) Orientation map (left) and pole figure (right) of a detrital shock-twinned zircon. Pole figure illustrates the 65°/<110> disorientation relation between the lamellar twins and the host zircon (data from the inset box) and is a lower-hemisphere, equal-area projection. Both images are in the same *x-y* reference frame. IPFx—inverse pole figure, x projection.

and dates listed in Table 2. Additionally, uncertainty associated with the U matrix correction was propagated in quadrature into $^{238}U/^{206}Pb^{*}$ ratios and dates. Common-Pb corrections were applied to all analyses using measured ^{204}Pb and the contemporaneous common Pb isotopic composition determined according to the model of Stacey and Kramers (1975). A secondary correction approach, using in-house standard XKIV (U = 740 ppm; age = 1080 Ma), was also employed to verify the matrix matching correction. Reduction of the data using this near-matrix-matched standard led to a similar regression through the unknown data with intercepts at 1643 ± 110 Ma and 2956 ± 13 Ma (mean square of weighted deviation [MSWD] = 2.5).

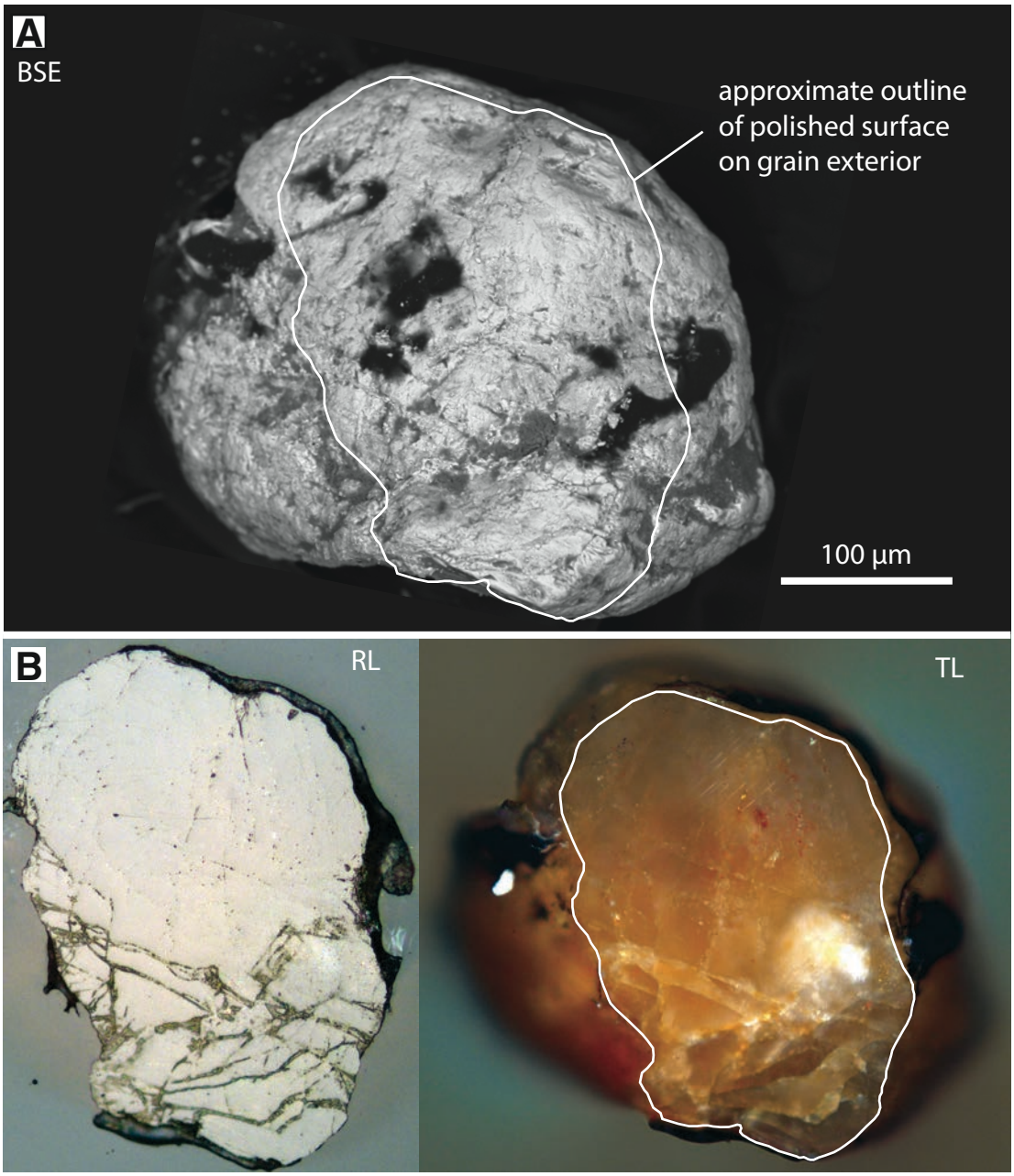

Figure 3. Images of detrital xenotime grain 14VD64-1. (A) Backscattered electron (BSE) image of the exterior surface of the grain prior to polishing. (B–C) Reflected light (RL) and transmitted light (TL) images of the polished section. The white outlines in A and C approximate the location of the polished surface. Scale bar in A applies to all images.

RESULTS

Deformation Microstructures

BSE images of the polished surface show that some areas are featureless, whereas other areas contain fractures, cracks, and various planar microstructures (Fig. 4). An EBSD orientation map reveals two distinct microstructural domains (Fig. 5A). The largest domain is characterized by the presence of discrete planar deformation bands (PDBs), and it is referred to as the "PDB domain." A smaller domain defined by an ~50-µm-wide intragrain deformation zone that contains most of the deformation twins is referred to as the "twin domain." When orientation data for the whole grain are plotted on pole figures, pronounced systematic dispersion of crystallographic poles is evident (Fig. 5B). Characteristics of each domain are discussed below.

TABLE 1. ELECTRON BACKSCATTER DIFFRACTION (EBSD) ANALYSIS CONDITIONS

Grain:	zircon 98	xenotime 1	x1-ROI	x1-ROI	x1-ROI
Figure:	2B	5	6A	6C	6D
Epoxy mount:	SA18	SA21	SA21	SA21	SA21
Acquisition speed (Hz)	60	40	40	40	40
Background (frames)	–	64	64	64	64
Binning	–	4 × 4	4 × 4	4 × 4	4 × 4
Gain	High	High	High	High	High
Hough resolution	60	60	60	60	60
Band detection minimum	11	11	11	11	11
Mean angular deviation	0.64	0.55	0.53	0.54	0.64
X steps	1878	480	134	102	121
Y steps	1419	576	94	122	95
Step size (nm)	80	600	75	50	100
Pixels in map	2,664,882	276,480	12,596	12,566	11,495
Time for collection (min)	140	500	31	32	29

Noise reduction applied to all maps: wildspike
Scanning electron microscope model: Tescan Mira3 field emission gun SEM
EBSD system:
Xenotime analyses (2017): Nordlys Nano Detector; AZtec.
Zircon analyses (2019): Oxford Symmetry detector; AZtec
Match units:
Xenotime (Y), Inorganic Crystal Structure Database (Milligan et al., 1982)
Zircon, Mincryst Card 5260 (Hazen and Finger, 1979)

The grains were mounted flat in epoxy and were grounded with Cu tape.
All samples were rotated to a 70° tilt by moving the stage.
Each sample was coated with a thin (<5 nm) carbon coat.
Accelerating voltage was 20 kV; working distance was from 20 to 25 mm.

PDB Domain

Orientation mapping reveals the presence of PDBs in different orientations, and also areas with no discernible PDBs (Fig. 5A). The regions without PDBs, some as large as ~100 µm by ~100 µm (Fig. 5A, upper right), record progressive strain with up to ~10° of cumulative misorientation. Three orientations of PDBs (Fig. 5A) accommodate crystal misorientation of up to 25° over discrete 1–5-µm-wide bands (Fig. 6A). All three sets of PDBs are commonly tapered and emanate from grain margins and interiors, extending for tens of micrometers. The three sets of PDBs exhibit various intersection relationships (Fig. 6A); however, it is difficult to conclusively determine the relative timing of their formation from features exposed on the polished surface. Traces of the planes for PDB 1 and PDB 3 can each be fit to a great circle that contains poles to (001) and {100} (Fig. 6B); these PDBs thus have orientations parallel to {100} and are interpreted to have formed by <100>{010} slip. The geometry of the host-PDB orientations is most consistent with tilt boundaries (Fig. 6E; Reddy et al., 2007). In domains where different PDB sets intersect, misorientations can reach up to 40° due to the opposite sense of misorientation, relative to the host grain, associated with each PDB set (Fig. 6A).

Twin Domain

The most conspicuous feature of the twin domain is that it manifests as an ~50-µm-wide intragrain zone of high strain that localized nearly all of the identified deformation twins and produced symmetrical displacement of the grain margin (Fig. 5A). Formation of this zone appears to postdate PDB formation, because bands of PDB 1 are strongly deflected into the twin zone with an apparent left-lateral sense on the polished surface (see Fig. 5A, lower boundary of twin zone). Two sets of deformation twin lamellae in {112} are each defined by 65° misorientation from the host grain around an axis parallel to <110> (Figs. 6C and 6D). Twin lamellae are generally <1 µm wide and polysynthetic (Fig. 6D). Locally, there are terminations of twin lamellae against PDBs (Fig. 6C); the consistent orientation of the PDBs at this interface as well as a small (<0.5 µm) gap between the twin and PDBs all indicate that PDB formation predates twin formation (Fig. 6C).

In Situ U-Pb Analyses

In total, 29 U-Pb analyses were made, including multiple analyses of all microstructural domains (Fig. 7A). The concentration of U ranged from 1932 to 3532 ppm (Table 2), which justified

TABLE 2. SECONDARY ION MASS SPECTROMETRY (SIMS) ANALYSES OF XENOTIME GRAIN 14VD64-1 FROM THE VREDEFORT DOME, SOUTH AFRICA

Spot no.	^{238}U (ppm)	^{232}Th (ppm)	^{232}Th/^{238}U	f204 (%)	^{238}U/^{206}Pb* (±1σ)		^{207}Pb*/^{206}Pb* (±1σ)		^{207}Pb*/^{206}Pb* date (Ma ± 1σ)		Disc. (%)
64-16	2574	297	0.12	0.011	1.7464	0.0408	0.2201	0.0005	2981	4	2
64-3	2003	283	0.14	0.013	1.6764	0.0393	0.2197	0.0010	2979	7	–1
64-2	2019	246	0.12	0.013	1.6722	0.0392	0.2192	0.0005	2975	4	–2
64-13	2518	395	0.16	0.008	1.6540	0.0385	0.2191	0.0005	2974	3	–2
64-17	2401	311	0.13	0.004	1.6684	0.0391	0.2188	0.0005	2972	4	–2
64-4	2263	287	0.13	0.011	1.6627	0.0441	0.2184	0.0005	2969	3	–2
64-12	2808	458	0.16	0.024	1.6811	0.0390	0.2184	0.0004	2969	3	–1
64-14	2670	414	0.16	0.008	1.7136	0.0399	0.2179	0.0005	2965	4	0
64-1	2469	302	0.12	0.028	1.7291	0.0402	0.2175	0.0008	2962	6	1
64-8	2164	393	0.18	0.012	1.7022	0.0440	0.2171	0.0005	2959	4	–1
64-15	2555	349	0.14	0.030	1.6904	0.0394	0.2167	0.0008	2956	6	–1
64-7	1968	150	0.08	0.078	1.6955	0.0400	0.2160	0.0006	2951	4	–1
64-11	2971	604	0.20	0.018	1.7513	0.0405	0.2159	0.0004	2950	3	1
64-9	2483	432	0.17	0.029	1.7442	0.0405	0.2158	0.0014	2949	11	1
64-19	2260	318	0.14	0.022	1.7643	0.0416	0.2157	0.0005	2949	4	2
64-6	2512	418	0.17	0.029	1.7193	0.0400	0.2157	0.0004	2949	3	0
64-10	2524	521	0.21	0.016	1.7742	0.0412	0.2144	0.0005	2939	4	2
64-31	1932	352	0.18	0.042	1.7608	0.0415	0.2125	0.0005	2925	4	1
64-5	2794	484	0.17	0.030	1.8029	0.0417	0.2124	0.0004	2924	3	3
64-28	2713	1087	0.40	0.040	1.8110	0.0420	0.2107	0.0005	2911	4	3
64-24	2281	357	0.16	0.058	1.7839	0.0418	0.2100	0.0005	2906	4	1
64-27	2662	623	0.23	0.067	1.8292	0.0425	0.2092	0.0005	2899	4	3
64-25	1938	309	0.16	0.075	1.7703	0.0417	0.2076	0.0008	2887	7	0
64-18	2893	710	0.25	0.042	1.8680	0.0518	0.2071	0.0015	2883	12	4
64-26	2226	452	0.20	0.026	1.8116	0.0426	0.2070	0.0005	2882	4	2
64-22	2257	393	0.17	0.096	1.9127	0.0447	0.2043	0.0005	2861	4	5
64-23	2343	437	0.19	0.118	1.8990	0.0443	0.1986	0.0005	2815	4	3
64-29	3445	1144	0.33	0.087	2.0560	0.0473	0.1915	0.0012	2755	11	7
64-30	3532	1528	0.43	0.140	2.4000	0.0554	0.1701	0.0017	2559	17	12

Note: Data are listed in decreasing ^{207}Pb/^{206}Pb age order. All isotope data were calibrated against concurrent analyses of XKARG, as described in the text. Isotope ratios include a matrix correction for U concentration. Concentrations are relative to XKIV with 740 ppm U. All listed Pb isotope data were corrected for common Pb using the measured ^{204}Pb and the composition of Stacy and Kramers (1975) for coeval Pb. Precisions are 1σ and include an external spot-to-spot (reproducibility) uncertainty of 0.88% (1σ) and a ^{238}U/^{206}Pb* calibration uncertainty of 0.37% (1σ) based on repeated analyses of XKARG during the analytical session. Additional uncertainty from U-based matrix correction was propagated in quadrature in the U/Pb ratios and dates. Disc. (%) is discordance = [(^{207}Pb*/^{206}Pb* age – ^{206}Pb*/^{238}U age)/(^{207}Pb*/^{206}Pb* age)] × 100.
*Refers to radiogenic Pb.

use of a U-based matrix correction, given that the Archean xenotime standard contains ~5000 ppm U. The U-Pb analyses ranged from concordant to variably discordant (Fig. 8), but data from each microstructural domain showed a large degree of overlap on concordia (Fig. 9A). Various possible correlations between age, [U], discordance, and band contrast (as a proxy for crystallinity) were evaluated (Fig. 8). Positive correlations between increasing [U] and discordance with decreasing age were found, as expected (Figs. 8A–8C). However, no correlations were observed for [U], discordance, or age with band contrast (Figs. 8D–8F), indicating a relatively consistent degree of crystallinity across all domains of the grain. EBSD analysis yielded high-quality diffraction data (Mean Angular deviation in degrees [MAD] values from 0.5 to 0.6; Table 1) across the grain, including all high-U spots, indicating that the grain is not metamict. Moreover, no correlation was detected between age and the various deformation microstructure (e.g., presence of twins or PDBs; Fig. 9A). A well-defined discordia regression through the full data set yielded an upper concordia intercept of 2953 ± 15 Ma (2σ, MSWD = 0.57) and an imprecise lower concordia intercept of 1754 ± 150 Ma.

DISCUSSION

Deformation Microstructures in Xenotime

Twins and PDBs in naturally deformed xenotime have only been reported in grains from confirmed impact structures; however, there are currently no experimental constraints with

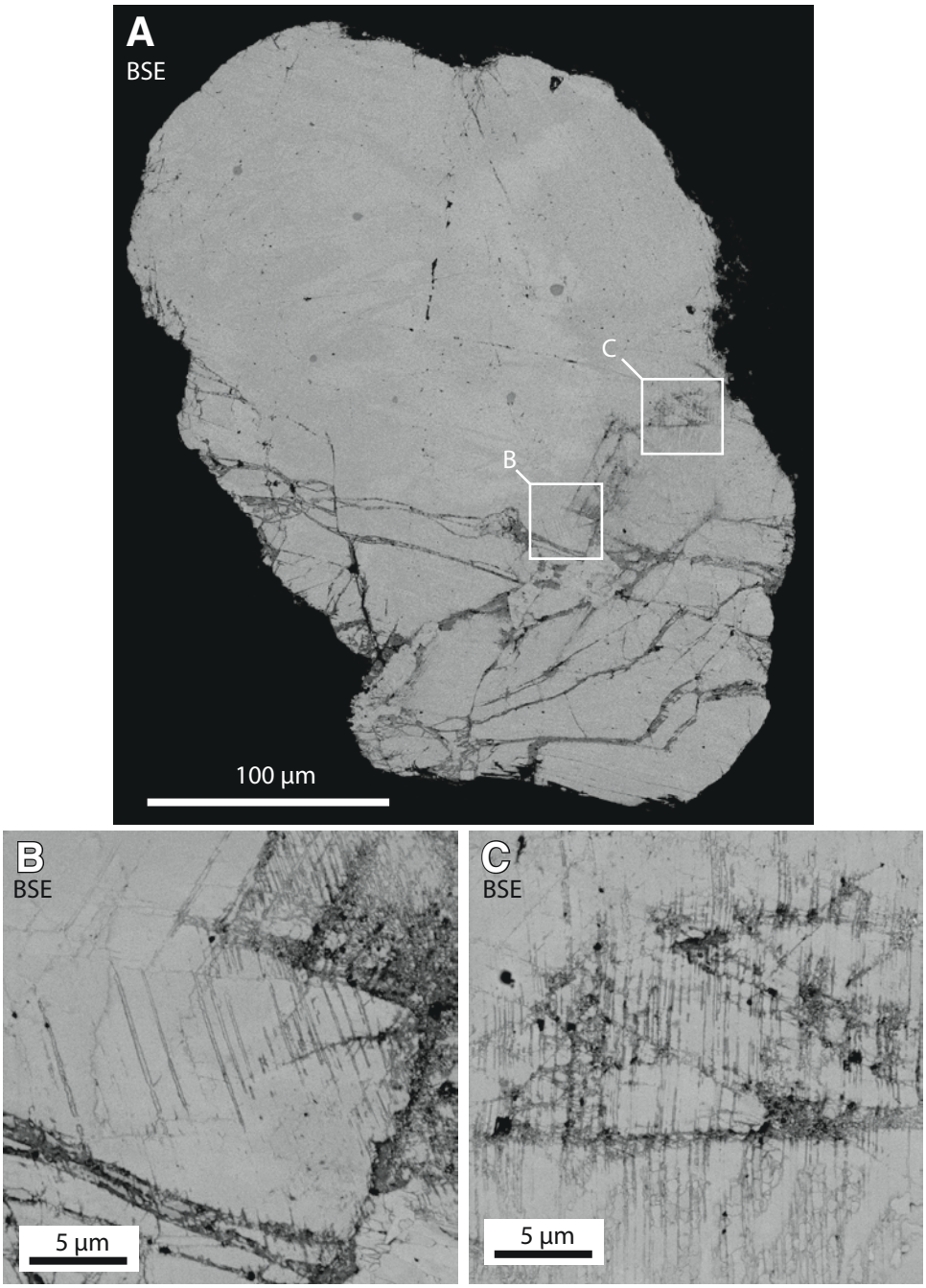

Figure 4. Backscattered electron (BSE) images of the polished section. (A) Full section image. (B–C) These insets show regions with closely spaced planar microstructures that were later revealed to be {112} lamellar deformation twins.

which to calibrate their formation conditions. The geometry of {112} deformation twins and {100} PDBs relative to the host grain in xenotime is seemingly identical to those found in shocked zircon. In zircon, {112} twins are diagnostic of shock deformation and have been reported from several impact environments (e.g., Moser et al., 2011; Timms et al., 2012; Erickson et al., 2013a; Thomson et al., 2014; Cavosie and Folco, this volume). PDBs in {100} also form in shocked zircon (e.g., Erickson et al., 2013a), but they are not diagnostic of impact processes, as they can occur in tectonically deformed zircon (Kovaleva et al., 2015).

The grain in this study bears some similarities to shocked xenotime grains described from the Santa Fe impact structure, which preserve diffuse PDBs in one orientation with ~5° of lattice misorientation and {112} deformation twins (Cavosie et al., 2016); shock-twinned zircon grains have also been reported from the Santa Fe impact structure (Montalvo et al., 2019). The xenotime grain studied here is also similar to a shock-twinned

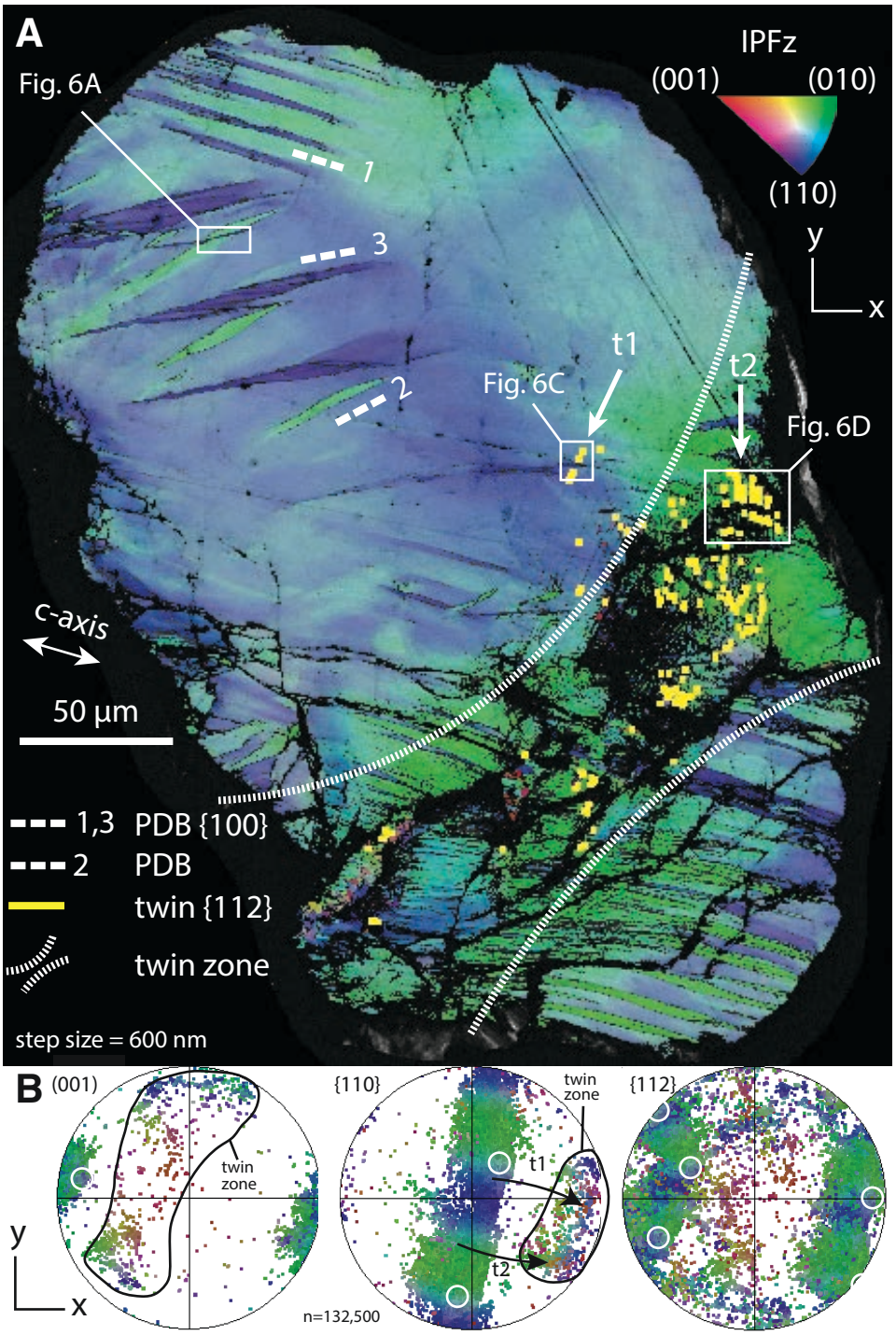

Figure 5. Electron backscatter diffraction data for the detrital shocked xenotime grain. (A) Orientation map (inverse pole figure [IPF], z projection) showing deformation features, including planar deformation bands (PDBs) and deformation twin lamellae (t). (B) Pole figures showing data from A (all are lower-hemisphere, equal-area projection). White circles in B show average orientation based on data contouring (not shown). Note clustering of (001) poles, and the continuous dispersion of poles to {110}.

xenotime grain included in a shocked quartz grain from the Spider impact structure (Cox et al., this volume). However, the Vredefort xenotime grain described here appears to record more intense deformation compared to those mentioned above, as it features the highest density of deformation twins thus far reported for xenotime, and three sets of PDBs with discrete boundaries and up to 40° of lattice misorientation across individual structures. The conspicuous deflection of PDBs into the twin zone in the Vredefort grain (Fig. 5A) suggests that formation of PDBs preceded formation of {112} deformation twins; however, it is plausible that all observed microstructures formed in rapid succession, either during propagation of shock waves early in the Vredefort impact event, or at the initiation of crater excavation (Melosh, 1989).

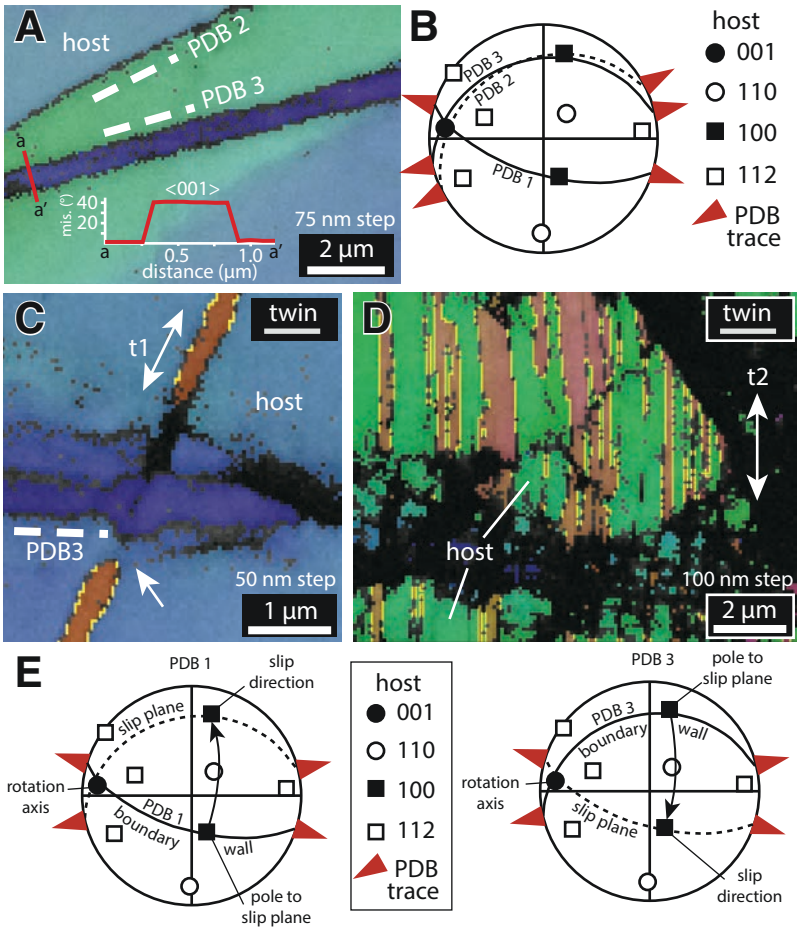

Figure 6. Deformation features in xenotime grain 14VD64-1. (A) Map showing planar deformation band (PDB) 3 crosscutting PDB 2; a profile across PDB 3 indicates up to 40° of misorientation (mis.) about <001>. (B) Pole figure showing that PDBs 1 and 3 contain a common <100> and are in an orientation consistent with {100}. The orientation of PDB 2 is a plane within ±10° of {100}. (C) Map showing that twin 1 terminates in the host prior to encountering PDB 3 (see arrow), and may postdate PDB formation. (D) Map of twin 2 from within the twin zone, showing polysynthetic lamellae. (E) Pole figures illustrating the inferred geometry of PDB 1 and PDB 3 as tilt boundaries (Reddy et al., 2007). The tilt boundary geometry indicated is consistent with formation of PDBs by <100>{010} slip systems.

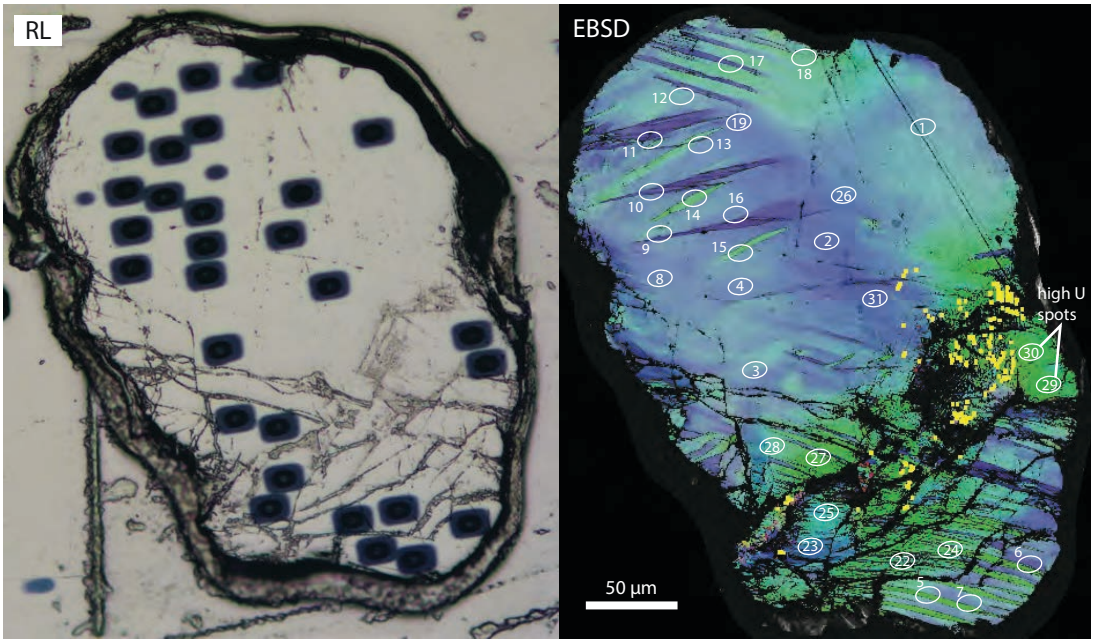

Figure 7. Location of secondary ion mass spectrometry (SIMS) (sensitive high-resolution ion microprobe [SHRIMP]) analysis spots. The reflected light (RL, left) image of the gold-coated sample shows the locations of the square raster boxes, with the central darker area representing the actual analysis spot. The orientation map (electron backscatter diffraction [EBSD], right) shows the analysis labels. The two highest-U spots (29 and 30) are annotated. See Figure 5 for details of the orientation map.

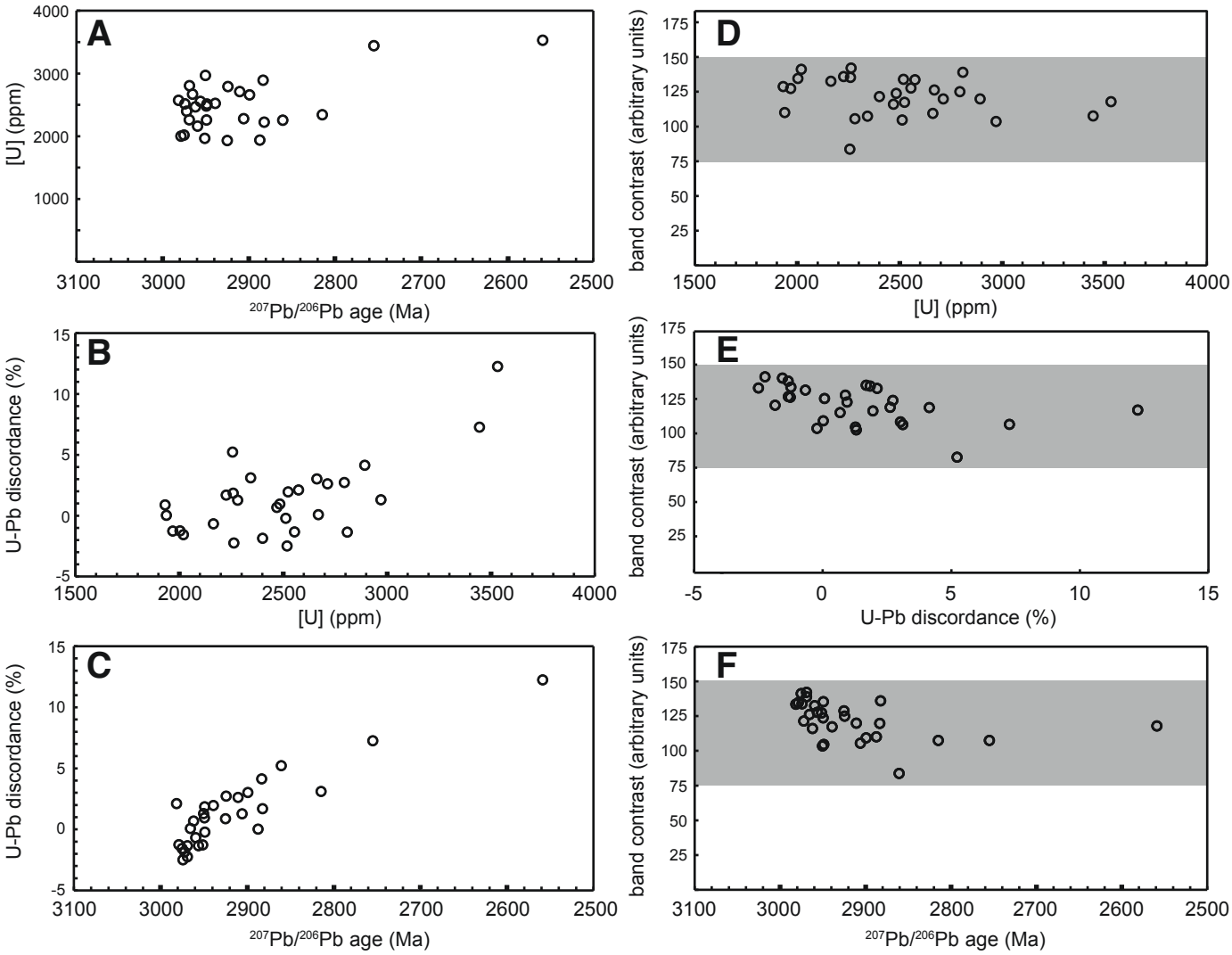

Figure 8. Bivariate diagrams showing relations among age, [U], U-Pb discordance, and band contrast for the secondary ion mass spectrometry (SIMS) analyses of xenotime grain 14VD64-1: (A) [U] vs. age; (B) discordance vs. [U]; (C) discordance vs. age; (D) band contrast vs. [U], (E) band contrast vs. discordance, and (F) band contrast vs. age. Shaded fields in D–E indicate the range of band contrast values, which were derived from electron backscatter diffraction (EBSD) data from the same spot locations that were measured by SIMS.

New Shocked Mineral at the Vredefort Dome

Shocked xenotime has not previously been reported at the Vredefort structure (Gibson and Reimold, 2008), and it provides further evidence of impact-related deformation. At Vredefort, shock microstructures have previously been reported in quartz (see references in Gibson and Reimold, 2008), zircon (e.g., Moser et al., 2011), and monazite (Erickson et al., 2017), and the high-pressure SiO_2 polymorphs coesite and stishovite have also been described (Martini, 1978). The 2953 ± 15 Ma upper-intercept age derived here for xenotime overlaps with ages of rocks across the core of the Vredefort structure, including ages of zircon grains from pseudotachylitic breccia and granophyre (Kamo et al., 1996; Wielicki and Harrison, 2015), and also ages of zircon grains in shocked granitoid basement rocks (Armstrong et al., 2006), but given its detrital nature, the grain may have originated elsewhere. If it originated in neighboring bedrock, then correlative-age regional basement rock on the Kaapvaal craton was likely the original source for the grain, prior to its pre-impact deposition in siliciclastic rocks now exposed in the collar (Fig. 1C). The occurrence of detrital shock-twinned zircon in the same sediment sample (Fig. 2) and in nearby samples (Fig. 1B) suggests that rocks near the sampling area may record impact pressures as high as ~20 GPa (e.g., Moser et al., 2011) if the zircon grains are locally derived. We note that the formation conditions of lamellar {112} deformation twins in zircon have yet to be calculated precisely (Cavosie and Folco, this volume).

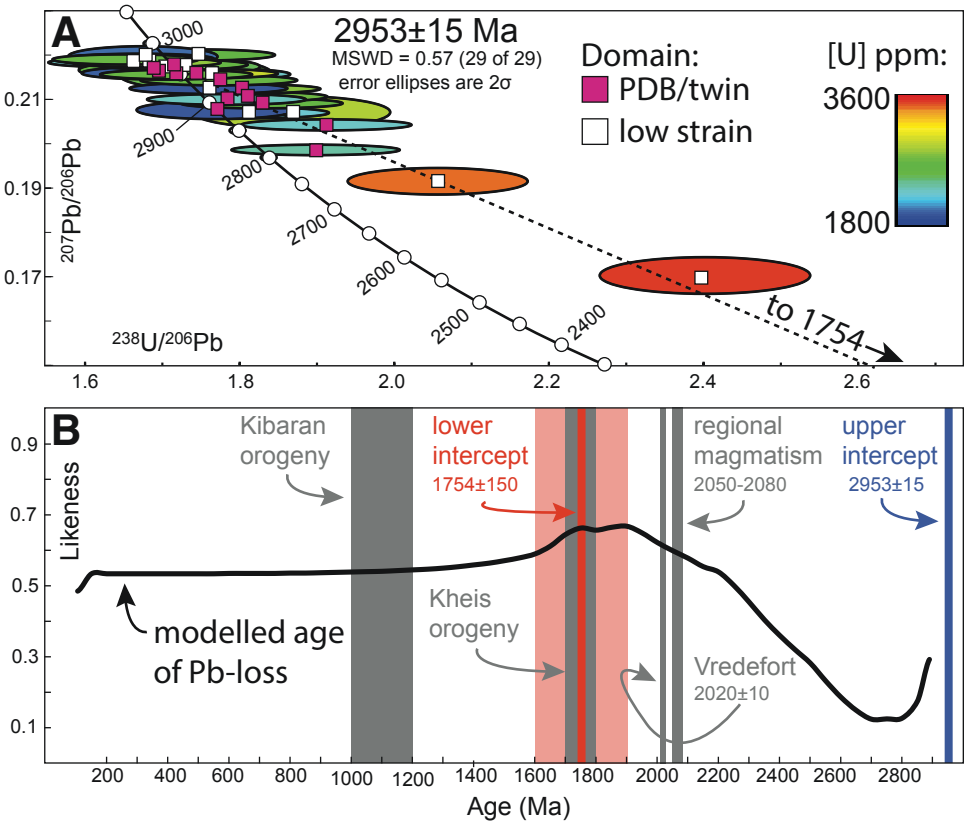

Figure 9. Summary of geochronology results. (A) Sensitive high-resolution ion microprobe (SHRIMP) U-Pb analyses for xenotime grain 14VD64-1 plotted on a Tera-Wasserburg concordia diagram. Data are color-coded by [U]; analyses from low-strain and high-strain (planar deformation band [PDB]/twin) domains are distinguished. (B) Modeled age of Pb loss based on a concordant-discordant comparison (CDC) test (Kirkland et al., 2017). The youngest peak in the broad maxima coincides with the concordia lower-intercept age of ca. 1750 Ma. The broadness of the maxima allows for the possibility of earlier Pb loss; however, there is no clear indication that it resulted from the Vredefort impact. The model provides no support for Pb loss related to the Mesoproterozoic Kibaran orogeny.

Significance of Pb Loss in Deformed Xenotime

Xenotime strongly partitions U into its structure; however, it is not known to accumulate radiation damage; consequently, U-Pb discordance in xenotime is uncommon (Hawkins and Bowring, 1997; Rasmussen, 2005). In the analyzed grain, Pb loss does not appear to correlate to any of the shock-induced microstructures, although there is an apparent link between age variation and [U] and discordance (Figs. 8A–8B). However, [U] variation across the grain is modest, from 2000 to 3000 ppm, with the two highest [U] spots only up to 3500 ppm (Fig. 8A), which is here assumed to result from growth zoning. The overall crystalline nature of all areas of the grain analyzed by SIMS (Figs. 8D–8F), even in areas that experienced demonstrable Pb loss (Fig. 9A), is attributed to self-annealing of radiation damage, as has been reported previously for xenotime (Meldrum et al., 1997; Urusov et al., 2012) and other phosphates, including apatite and monazite (e.g., Gleadow et al., 2003). In the case of the studied xenotime grain, the deformation microstructures do not appear to have acted as fast diffusion pathways for Pb at the time of their formation (e.g., the Vredefort impact at ca. 2020 Ma).

In order to better understand what may be a pattern of cryptic Pb loss within this grain, we carried out a concordant-discordant comparison (CDC) test (Kirkland et al., 2017). The CDC test applies a Bayesian approach by taking the oldest concordant age as a priori information on the initial growth of the grain and constructing a modeled age population for every possible time of Pb loss (in this case, from 0 to 3000 Ma) in 50 m.y. steps for all other data points. In doing so, we evaluated the most likely time of Pb loss assuming an initial genetic relationship between different parts of the grain. A similarity test between each modeled population (Satkoski et al., 2013), for a given time of Pb loss, and the oldest age allows an evaluation of the most likely time of Pb mobility (Fig. 9B). This approach has better power at resolving multiple Pb-loss events than a single linear regression.

The CDC result showed a broad maxima in "likeness" of modeled age spectra, with a peak centered at ca. 1750 Ma that coincides with the concordia lower-intercept age (Fig. 9B). The broadness of the modeled Pb-loss age maxima allows for the possibility that the grain may have experienced somewhat earlier Pb loss, but it does not provide direct evidence that it was caused by the ca. 2020 Ma impact (Fig. 9B). The model results further provide no support for a multiple Pb-loss scenario during the ca. 1100 Ma Kibaran orogeny (Fig. 9B; Thomas et al., 1994). The excellent fit of the discordia curve (MSWD = 0.57) for the entire data set (n = 29) is therefore most consistent with one episode of partial Pb loss at ca. 1750 Ma (Figs. 9A and 9B).

Loss of radiogenic Pb at ca. 1750 ± 150 Ma is too young to have been caused by the ca. 2020 Ma Vredefort impact, which is significant for two reasons. First, it indicates that shock deformation in xenotime, including twin and PDB formation, did not reset the U-Pb system during their formation at the scale of the ~10 µm

domains measured by SIMS. In this regard, the U-Pb system in shock-twinned xenotime is thus similar to that in shock-twinned zircon, where Pb loss does not record the age of impact (e.g., Erickson et al., 2013b; Cavosie et al., 2015, 2018; Montalvo et al., 2017; Montalvo et al., 2019). Second, radioisotope ages of ca. 1750 Ma from minerals or whole rock (e.g., U-Pb or $^{40}Ar/^{39}Ar$ geochronology) are uncommon around the Vredefort Dome or the greater Witwatersrand basin. However, 1800–1700 Ma ages associated with the Kheis orogeny have been reported in terranes of the Namaqua-Natal Belt that girdle the western margin of the Kaapvaal craton (Eglington, 2006; van Niekerk and Beukes, 2019). More locally, a few ^{40}Ar-^{39}Ar ages of ca. 1700 Ma for mica within the Vredefort Dome have been reported, and tentatively attributed to partial resetting events (Reimold et al., 1996), perhaps also related to the Kheis orogeny. This leads to the possibility that, despite a large uncertainty, the lower-intercept age carries geological significance and records a poorly understood alteration episode in the Witwatersrand basin.

Results presented here provide the first in-depth study of Pb-loss patterns and behavior in highly strained xenotime. Our results suggest that previously published xenotime U-Pb data from other high-strain environments that feature complex age spectra and exhibit discordance, such as grains from shear zones (e.g., Hawkins and Bowring, 1997), may have been influenced by, and be recording, more protracted geological histories that can be revealed through a combination of microstructural characterization and targeted U-Pb geochronology.

ACKNOWLEDGMENTS

B. Hess, A. Kennedy, and S. Montalvo provided assistance. Support was provided by a grant from the U.S. National Science Foundation to Cavosie (EAR-1145118), a Curtin Research Fellowship, the Space Science Technology Centre (SSTC), The Institute of Geological Research (TIGeR), and the John de Laeter Centre (JdLC) at Curtin University. We thank volume editor W.U. Reimold for editorial handling, and M. Wielicki and G. Kenny for detailed reviews.

REFERENCES CITED

Armstrong, R.A., Lana, C., Reimold, W.U., and Gibson, R.L., 2006, SHRIMP zircon age constraints on Mesoarchean crustal development in the Vredefort Dome, central Kaapvaal craton, South Africa, *in* Reimold, W.U., and Gibson, R.L., eds., Processes on the Early Earth: Geological Society of America Special Paper 405, p. 233–253, https://doi.org/10.1130/2006.2405(13).

Bischoff, A.A., Mayer, J.J., Voors, W.A., and Retief, P.F., 1999, Geology of the Vredefort Dome: Pretoria, South Africa, Council for Geoscience, 49 p. and map scale 1:50,000.

Carter, N.L., 1965, Basal quartz deformation lamellae—A criterion for recognition of impactites: American Journal of Science, v. 263, p. 786–806, https://doi.org/10.2475/ajs.263.9.786.

Cavosie, A.J., and Folco, L., 2021, this volume, Shock-twinned zircon in ejecta from the 45-m-diameter Kamil crater in southern Egypt, *in* Reimold, W.U., and Koeberl, C., eds., Large Meteorite Impacts and Planetary Evolution VI: Geological Society of America Special Paper 550, https://doi.org/10.1130/2021.2550(17).

Cavosie, A.J., Quintero, R.R., Radovan, H.A., and Moser, D.E., 2010, A record of ancient cataclysm in modern sand: Shock microstructures in detrital minerals from the Vaal River, Vredefort Dome, South Africa: Geological Society of America Bulletin, v. 122, p. 1968–1980, https://doi.org/10.1130/B30187.1.

Cavosie, A.J., Erickson, T.M., Timms, N.E., Reddy, S.M., Talavera, C., Montalvo, S.D., Pincus, M.R., Gibbon, R.J., and Moser, D., 2015, A terrestrial perspective on using ex situ shocked zircons to date lunar impacts: Geology, v. 43, p. 999–1002, https://doi.org/10.1130/G37059.1.

Cavosie, A.J., Montalvo, P.E., Timms, N.E., and Reddy, S.M., 2016, Nanoscale deformation twinning in xenotime, a new shocked mineral, from the Santa Fe impact structure (New Mexico, U.S.A.): Geology, v. 44, p. 803–806, https://doi.org/10.1130/G38179.1.

Cavosie, A.J., Erickson, T.M., Montalvo, P.E., Prado, D.C., Cintron, N.O., and Gibbon, R.J., 2018, The Rietputs Formation in South Africa: A Pleistocene fluvial archive of meteorite impact unique to the Kaapvaal craton, *in* Moser, D.E., Corfu, F., Reddy, S.M., Darling, J., and Tait, K., eds., Microstructural Geochronology; Lattice to Atom-Scale Records of Planetary Evolution: American Geophysical Union Geophysical Monograph 232, p. 203–224, https://doi.org/10.1002/9781119227250.ch9.

Cherniak, D.J., 2006, Pb and rare earth element diffusion in xenotime: Lithos, v. 88, p. 1–14, https://doi.org/10.1016/j.lithos.2005.08.002.

Cox, M.A., Cavosie, A.J., Poelchau, M., Kenkmann, T., Bland, P.A., and Miljković, K., 2021, this volume, Shock deformation microstructures in xenotime from the Spider impact structure, Western Australia, *in* Reimold, W.U., and Koeberl, C., eds., Large Meteorite Impacts and Planetary Evolution VI: Geological Society of America Special Paper 550, https://doi.org/10.1130/2021.2550(19).

Eglington, B.M., 2006, Evolution of the Namaqua-Natal Belt, southern Africa—A geochronological and isotope geochemical review: Journal of African Earth Sciences, v. 46, p. 93–111, https://doi.org/10.1016/j.jafrearsci.2006.01.014.

Erickson, T.M., Cavosie, A.J., Moser, D.E., Barker, I.R., and Radovan, H.A., 2013a, Correlating planar microstructures in shocked zircon from the Vredefort Dome at multiple scales: Crystallographic modelling, external and internal imaging, and EBSD structural analysis: The American Mineralogist, v. 98, p. 53–65, https://doi.org/10.2138/am.2013.4165.

Erickson, T.M., Cavosie, A.J., Moser, D.E., Barker, I.R., Radovan, H.A., and Wooden, J., 2013b, Identification and provenance determination of distally transported, Vredefort-derived shocked minerals in the Vaal River, South Africa, using SEM and SHRIMP-RG techniques: Geochimica et Cosmochimica Acta, v. 107, p. 170–188, https://doi.org/10.1016/j.gca.2012.12.008.

Erickson, T.M., Cavosie, A.J., Pearce, M.A., Timms, N.E., and Reddy, S.M., 2016, Empirical constraints on shock features in monazite using shocked zircon inclusions: Geology, v. 44, p. 635–638, https://doi.org/10.1130/G37979.1.

Erickson, T.M., Timms, N.E., Kirkland, C.L., Tohver, E., Cavosie, A.J., Pearce, M.A., and Reddy, S.M., 2017, Shocked monazite chronometry: Integrating microstructural and in situ isotopic age data for determining precise impact ages: Contributions to Mineralogy and Petrology, v. 172, p. 11, https://doi.org/10.1007/s00410-017-1328-2.

Fletcher, I.R., McNaughton, N.J., Aleinikoff, J.A., Rasmussen, B., and Kamo, S.L., 2004, Improved calibration procedures and new standards for U-Pb and Th-Pb dating of Phanerozoic xenotime by ion microprobe: Chemical Geology, v. 209, p. 295–314, https://doi.org/10.1016/j.chemgeo.2004.06.015.

Gibson, R.L., and Reimold, W.U., 2005, Shock pressure distribution in the Vredefort impact structure, South Africa, *in* Kenkmann, T., Hörz, F., and Deutsch, A., eds., Large Meteorite Impacts III: Geological Society of America Special Paper 384, p. 329–349, https://doi.org/10.1130/0-8137-2384-1.329.

Gibson, R.L., and Reimold, W.U., 2008, Geology of the Vredefort Impact Structure: A Guide to Sites of Interest: Pretoria, South Africa, Council of Geoscience Memoir 97, 181 p.

Gibson, R.L., Armstrong, R.A., and Reimold, W.U., 1997, The age and thermal evolution of the Vredefort impact structure: A single-grain U-Pb zircon study: Geochimica et Cosmochimica Acta, v. 61, p. 1531–1540, https://doi.org/10.1016/S0016-7037(97)00013-6.

Gleadow, A.J.W., Belton, D.X., Kohn, B.P., and Brown, R.W., 2003, Fission track dating of phosphate minerals the thermochronology of apatite:

Reviews in Mineralogy and Geochemistry, v. 48, no. 1, p. 579–630, https://doi.org/10.2138/rmg.2002.48.16.

Grieve, R.A.F., Coderre, J.M., Roberston, P.B., and Alexopolous, J., 1990, Microscopic planar deformation features in quartz of the Vredefort structure: Anomalous but still suggestive of an impact origin: Tectonophysics, v. 171, p. 185–200, https://doi.org/10.1016/0040-1951(90)90098-S.

Hawkins, D.P., and Bowring, S.A., 1997, U-Pb systematics of monazite and xenotime: Case studies from the Paleoproterozoic of the Grand Canyon, Arizona: Contributions to Mineralogy and Petrology, v. 127, p. 87–103, https://doi.org/10.1007/s004100050267.

Hay, R.S., Mogilevsky, P., and Boakye, E., 2013, Phase transformations in xenotime rare-earth orthophosphate: Acta Materialia, v. 61, p. 6933–6947, https://doi.org/10.1016/j.actamat.2013.08.005.

Hazen, R.M., and Finger, L.W., 1979, Crystal structure and compressibility of zircon at high pressure: The American Mineralogist, v. 64, p. 196–201.

Kamo, S.L., Reimold, W.U., Krogh, T.E., and Colliston, W.P., 1996, A 2.023 Ga age for the Vredefort impact event and a first report of shocked metamorphosed zircon in pseudotachylytic breccias and granophyre: Earth and Planetary Science Letters, v. 144, p. 369–387, https://doi.org/10.1016/S0012-821X(96)00180-X.

Kirkland, C.L., Abello, F., Danišík, M., Gardiner, N.J., and Spencer, C., 2017, Mapping temporal and spatial patterns of zircon U-Pb disturbance: A Yilgarn craton case study: Gondwana Research, v. 52, p. 39–47, https://doi.org/10.1016/j.gr.2017.08.004.

Kovaleva, E., Klötzli, U., Habler, G., and Wheeler, J., 2015, Planar microstructures in zircon from paleo-seismic zones: The American Mineralogist, v. 100, p. 1834–1847, https://doi.org/10.2138/am-2015-5236.

Martini, J.E.J., 1978, Coesite and stishovite in the Vredefort Dome, South Africa: Nature, v. 272, p. 715–717, https://doi.org/10.1038/272715a0.

Meldrum, A., Boatner, L.A., and Ewing, R.C., 1997, Displacive radiation effects in the monazite- and zircon-structure orthophosphates: Physical Review B, v. 56, no. 21, p. 13805–13814, https://doi.org/10.1103/PhysRevB.56.13805.

Melosh, H.J., 1989, Impact Cratering: A Geologic Process: Oxford Monographs on Geology and Geophysics 11, 245 p.

Milligan, W.O., Mullica, D.F., Beall, G.W., and Boatner, L.A., 1982, Structural investigations of YPO_4, $ScPO_4$, and $LuPO_4$: Inorganica Chimica Acta, v. 60, p. 39–43, https://doi.org/10.1016/S0020-1693(00)91148-4.

Montalvo, S.D., Cavosie, A.J., Erickson, T.M., and Talavera, C., 2017, Fluvial transport of impact evidence from cratonic interior to passive margin: Vredefort-derived shocked zircon on the Atlantic coast of South Africa: The American Mineralogist, v. 102, no. 4, p. 813–823, https://doi.org/10.2138/am-2017-5857CCBYNCND.

Montalvo, P.E., Cavosie, A.J., Kirkland, C.L., Evans, N.J., McDonald, B.J., Talavera, C., Erickson, T.M., and Lugo-Centeno, C., 2019, Detrital shocked zircon provides first radiometric age constraint (<1472 Ma) for the Santa Fe impact structure, New Mexico, USA: Geological Society of America Bulletin, v. 131, p. 845–863, https://doi.org/10.1130/B31761.1.

Moser, D.E., 1997, Dating the shock wave and thermal imprint of the giant Vredefort impact, South Africa: Geology, v. 25, p. 7–10, https://doi.org/10.1130/0091-7613(1997)025<0007:DTSWAT>2.3.CO;2.

Moser, D.E., Cupelli, C.L., Barker, I.R., Flowers, R.M., Bowman, J.R., Wooden, J., and Hart, R.J., 2011, New zircon shock phenomena and their use for dating and reconstruction of large impact structures revealed by electron nanobeam (EBSD, CL, EDS) and isotopic U-Pb and (U-Th)/He analysis of the Vredefort Dome: Canadian Journal of Earth Sciences, v. 48, p. 117–139, https://doi.org/10.1139/E11-011.

Rasmussen, B., 2005, Radiometric dating of sedimentary rocks: The application of diagenetic xenotime geochronology: Earth-Science Reviews, v. 68, p. 197–243, https://doi.org/10.1016/j.earscirev.2004.05.004.

Reddy, S.M., Timms, N.E., Pantleon, W., and Trimby, P., 2007, Quantitative characterization of plastic deformation of zircon and geological implications: Contributions to Mineralogy and Petrology, v. 153, p. 625–645, https://doi.org/10.1007/s00410-006-0174-4.

Reimold, W.U., Gibson, R.L., and Layer, P.W., 1996, Further ^{40}Ar-^{39}Ar step-heating dating of fault rocks and metamorphic minerals from the Vredefort Dome and Witwatersrand basin: 27th Annual Lunar and Planetary Science Conference, abstract 1067.

Satkoski, A.M., Wilkinson, B.H., Hietpas, J., and Samson, S.D., 2013, Likeness among detrital zircon populations—An approach to the comparison of age frequency data in time and space: Geological Society of America Bulletin, v. 125, p. 1783–1799, https://doi.org/10.1130/B30888.1.

Stacey, J.S. and Kramers, J.D., 1975, Approximation of terrestrial lead isotope evolution by a two-stage model: Earth and Planetary Science Letters, v. 26, no. 2, p. 207–221, https://doi.org/10.1016/0012-297 821X(75)90088–6.

Thomas, R.J., Agenbacht, A.L.D., Cornell, D.H., and Moore, J.M., 1994, The Kibaran of southern Africa: Tectonic evolution and metallogeny: Ore Geology Reviews, v. 9, p. 131–160, https://doi.org/10.1016/0169-1368(94)90025-6.

Thomson, O.A., Cavosie, A.J., Moser, D.E., Barker, I., Radovan, H.A., and French, B.M., 2014, Preservation of detrital shocked minerals derived from the 1.85 Ga Sudbury impact structure in modern alluvium and Holocene glacial deposits: Geological Society of America Bulletin, v. 126, p. 720–737, https://doi.org/10.1130/B30958.1.

Timms, N.E., Reddy, S.M., Healy, D., Nemchin, A.A., Grange, M.L., Pidgeon, R.T., and Hart, R., 2012, Resolution of impact-related microstructures in lunar zircon: A shock-deformation mechanism map: Meteoritics & Planetary Science, v. 47, p. 120–141, https://doi.org/10.1111/j.1945-5100.2011.01316.x.

Urusov, V.S., Grechanovsky, A.E., and Eremin, N.N., 2012, Radiation resistance of the xenotime YPO4 from the computer simulation data: Glass Physics and Chemistry, v. 38, p. 55–62, https://doi.org/10.1134/S1087659612010178.

van Niekerk, H.S., and Beukes, N.J., 2019, Revised definition/outline of the Kheis terrane along the western margin of the Kaapvaal craton and lithostratigraphy of the newly proposed Keis Supergroup: South African Journal of Geology, v. 122, p. 187–220, https://doi.org/10.25131/sajg.122.0014.

Wielicki, M.M., and Harrison, T.M., 2015, Zircon formation in impact melts: Complications for deciphering planetary impact histories, *in* Osinski, G.R., and Kring, D.A., eds., Large Meteorite Impacts and Planetary Evolution V: Geological Society of America Special Paper 518, p. 127–134, https://doi.org/10.1130/2015.2518(08).

Wilkinson, T.M., Wu, D., Musselman, M.A., Li, N., Mara, N., and Packard, C.E., 2017, Mechanical behavior of rare-earth orthophosphates near the monazite/xenotime boundary characterized by nanoindentation: Materials Science and Engineering A, v. 691, p. 203–210, https://doi.org/10.1016/j.msea.2017.03.041.

Manuscript Accepted by the Society 20 November 2020
Manuscript Published Online xx Month 2021